

Liquid Metal-Enabled Tunable Synthesis of Nanoporous Polycrystalline Copper for Selective CO₂-to-Formate Electrochemical Conversion

Wenyu Zhong, Yuan Chi,* Ruohan Yu, Charlie Kong, Shujie Zhou, Chen Han, Jitraporn Vongsvivut, Guangzhao Mao, Kourosch Kalantar-Zadeh, Rose Amal, Jianbo Tang,* and Xunyu Lu*

Copper-based catalysts exhibit high activity in electrochemical CO₂ conversion to value-added chemicals. However, achieving precise control over catalysts design to generate narrowly distributed products remains challenging. Herein, a gallium (Ga) liquid metal-based approach is employed to synthesize hierarchical nanoporous copper (HNP Cu) catalysts with tailored ligament/pore and crystallite sizes. The nanoporosity and polycrystallinity are generated by dealloying intermetallic CuGa₂ formed after immersing pristine Cu foil in liquid Ga in a basic or acidic solution. The liquid metal-based approach allows for the transformation of monocrystalline Cu to the polycrystalline HNP Cu with enhanced CO₂ reduction reaction (CO₂RR) performance. The dealloyed HNP Cu catalyst with suitable crystallite size (22.8 nm) and nanoporous structure (ligament/pore size of 45 nm) exhibits a high Faradaic efficiency of 91% toward formate production under an applied potential as low as $-0.3 V_{RHE}$. The superior CO₂RR performance can be ascribed to the enlarged electrochemical catalytic surface area, the generation of preferred Cu facets, and the rich grain boundaries by polycrystallinity. This work demonstrates the potential of liquid metal-based synthesis for improving catalysts performance based on structural design, without increasing compositional complexity.

1. Introduction

The atmospheric concentration of carbon dioxide (CO₂) has increased by over 20% since 1975^[1] thereby intensifying the pressing issues such as global warming and the frequent occurrence of extreme weather events. In response to this challenge, electrochemical transformation of CO₂ to value-added chemicals and fuels not only addresses these environmental issues and reduces dependence on fossil fuels, but also establishes a pathway for the sustainable green fuel production. Formic acid (HCOOH) is considered as one of the high-value commodity chemicals among the CO₂ reduction products due to its wide industrial applications.^[2] Electrochemical conversion of CO₂ is an alternative pathway to conventional gas-phase CO-based synthesis of HCOOH.^[3]

Electrochemical conversion of CO₂ to HCOOH predominantly relies on using p-block metals such as tin (Sn), bismuth (Bi),

W. Zhong, Y. Chi, R. Yu, S. Zhou, C. Han, G. Mao, K. Kalantar-Zadeh, R. Amal, J. Tang, X. Lu
School of Chemical Engineering
University of New South Wales
Sydney, NSW 2052, Australia
E-mail: yuan.chi@unsw.edu.au; jianbo.tang@unsw.edu.au;
xunyu.lu@unsw.edu.au

C. Kong
Electron Microscope Unit
University of New South Wales
Sydney, NSW 2052, Australia
J. Vongsvivut
Infrared Microspectroscopy (IRM) Beamline
ANSTO-Australian Synchrotron
Clayton, VIC 3168, Australia
K. Kalantar-Zadeh
School of Chemical and Biomolecular Engineering
University of Sydney
Darlington, NSW 2008, Australia

 The ORCID identification number(s) for the author(s) of this article can be found under <https://doi.org/10.1002/smll.202403939>

© 2024 The Author(s). Small published by Wiley-VCH GmbH. This is an open access article under the terms of the [Creative Commons Attribution-NonCommercial-NoDerivs](#) License, which permits use and distribution in any medium, provided the original work is properly cited, the use is non-commercial and no modifications or adaptations are made.

DOI: 10.1002/smll.202403939

and indium (In) since their inherent oxyphilic nature facilitates the formation of *OCHO intermediate,^[4] a step essential for HCOOH production. However, the relative high cost,^[5] low electrical conductivity,^[6] and poor stability^[7] of p-block metals limit their practical uses, and therefore drove the interests in developing other HCOOH-selective metal-based catalysts. Copper (Cu) based catalysts are considered unique for electrochemical CO₂ reduction reactions (CO₂RR) as they are capable of producing a variety of liquid-phase products such as HCOOH, methanol (CH₃OH), and ethanol (C₂H₅OH).^[8] However, a significant challenge in Cu catalysts design is to achieve high selectivity toward a specific product, which would otherwise lead to the need for secondary separation and purification processes. Different strategies have been employed to enhance the selectivity and activity of Cu-based materials. Many of them such as alloying^[9] and element doping^[10] require introducing one or more foreign components, which can lead to issues in compositional control, active site design, and achieving long-term stability. Therefore, viable strategies that are able to improve catalysts design without increasing compositional complexity are highly desirable.

Nanostructured Cu-based materials have shown potential in achieving relatively high selectivity toward specific products during CO₂RR as the nanostructures and crystalline characteristics of Cu-based catalysts can have a considerable impact on the catalytic activity and reaction route selection during CO₂RR.^[11] For instance, research by Broekmann et al.,^[12] and Schmid et al.,^[13] show that Cu with nano-dendritic structure can provide an increased number of low-coordinated sites and exhibit larger electrochemical active surface area (ECSA), and these structural advantages then translate to improved activity and selectivity in CO₂RR, particularly toward the production of hydrocarbons such as ethylene (C₂H₄) and various alcohols. Moreover, modifying the local reaction environment is proven to be effective in enhancing the CO₂RR selectivity, which is achievable through the design of Cu-based catalysts with specific nano-morphologies. Smith et al.,^[14] demonstrated that by manipulating the length and the density of Cu nanowires, the selectivity toward C₂H₄ can be optimized. This is because longer and denser Cu nanowires create a local environment with a higher pH, which is conducive to C-C coupling reactions, thereby improving selectivity toward desired products. Besides, Cu materials with highly porous structures can also improve the CO₂RR selectivity through the effective confinement of reactive intermediates. Palmore et al.,^[15] fabricated a microporous Cu foam with nano-dendritic structures via electrodeposition, leading to an enhanced selectivity for HCOOH when compared to smooth surfaced Cu, as the nanoporous structure facilitates the confinement of *COOH intermediate.

Despite previous advancements in crafting Cu catalysts with different nanostructures, there still lacks practical strategies capable of fine-tuning the multiscale nanostructures in a controlled manner. Conventional methods that allow for uniform and controllable fabrication of porous structure such as chemical dealloying and vapor dealloying always require severe reaction conditions^[16] and a complicated precursor preparation process.^[17] Therefore, energy-efficient preparation methods for nanoporous catalysts are highly desired. Metal fine structure synthesis via the emerging liquid metal solvent-based approach is promising for achieving nanoscale structural control.^[18] Liquid metals such as gallium (Ga, melting point 29.8 °C) can serve as

metallic solvents for alloying with a wide variety of metals and forming intermetallic crystals at or near room temperatures.^[19] An electrochemical dealloying step can further remove the less noble Ga and creates bicontinuous hierarchical nanoporous (HNP) structures of the target metals.^[20] Apart from significantly reducing the temperature for fabricating master alloys, this liquid metal-assisted method can realize effective dealloying in a mild electrolyte and at low (even negative) dealloying potentials,^[20] since Ga is prone to oxidation. Therefore, it is feasible to choose a wide range of dealloying potentials to regulate nano porosity formation. In addition, Ga is an amphoteric metal that is able to be dealloyed by both acidic and alkaline etchants. Given that the dealloying solution has considerable influence on surface diffusion and electrochemical activities during nanoscale construction, the employment of liquid metal Ga can further allow the dealloy solution to be varied for structure tuning. In this regard, the liquid metal-enabled approach can offer multi-facet advantages that are not accessible with conventional methods.

Inspired by the liquid-metal derived nanoporous-structure synthesize and the well-acknowledged fact that the CO₂RR performance of Cu-based catalysts can be very sensitive to their morphology and structure, here in this work, a liquid metal-based strategy is demonstrated for fabricating self-supported HNP Cu catalysts with fine-tune ligament (pore) and crystallite sizes for CO₂RR. The HNP Cu catalysts show high CO₂-to-formate conversion performance, which is attributed by the enlarged ECSA and polycrystallinity. A high Faradaic efficiency (FE) of 91% toward formate production is achieved under a low potential of $-0.3 V_{RHE}$ (potential vs. reversible hydrogen electrode). The influence of nanoscale structural control (crystallite and nanoporous network) on the CO₂RR performance is thoroughly investigated.

2. Results and Discussion

2.1. Material and Characterization

The proposed liquid metal-based method is able to transform Cu foils into bicontinuous porous nanostructures (**Figure 1a**, Experimental Section 4.1). During the fabrication of the HNP Cu, the liquid Ga interacts and reacts with the pristine Cu surface to form an intermetallic CuGa₂ layer at 100 °C through continuous intermetallic formation and diffusion (**Figure S1**, Supporting Information). These intermetallic crystals form the first-level porosity. After a 12-h growth at 100 °C, the tetragonal CuGa₂ crystals show an average size of slightly over 10 μm (**Figure S2**, Supporting Information). After the intermetallic growth, the electrochemical dealloying step selectively dissolves the less noble Ga component in the intermetallic crystals, while the remaining Cu reconstructs to form the bicontinuous nanoporous network (the second-level porosity). A negative dealloying potential (vs. SCE), which is much lower than that commonly used in other dealloying systems,^[21] is able to realize effective Ga removal.

We find that both the dealloying potential and the dealloying (etching) solution affect the dealloying time and the characteristic (ligament and pore) sizes of the obtained nanoporous structures. The chronoamperometric curves of the samples show that the dealloying process is relatively fast, which can be completed in a period varying from ≈20 to 120 min depending on the dealloying conditions (**Figure 1b**). Ligament sizes of the samples

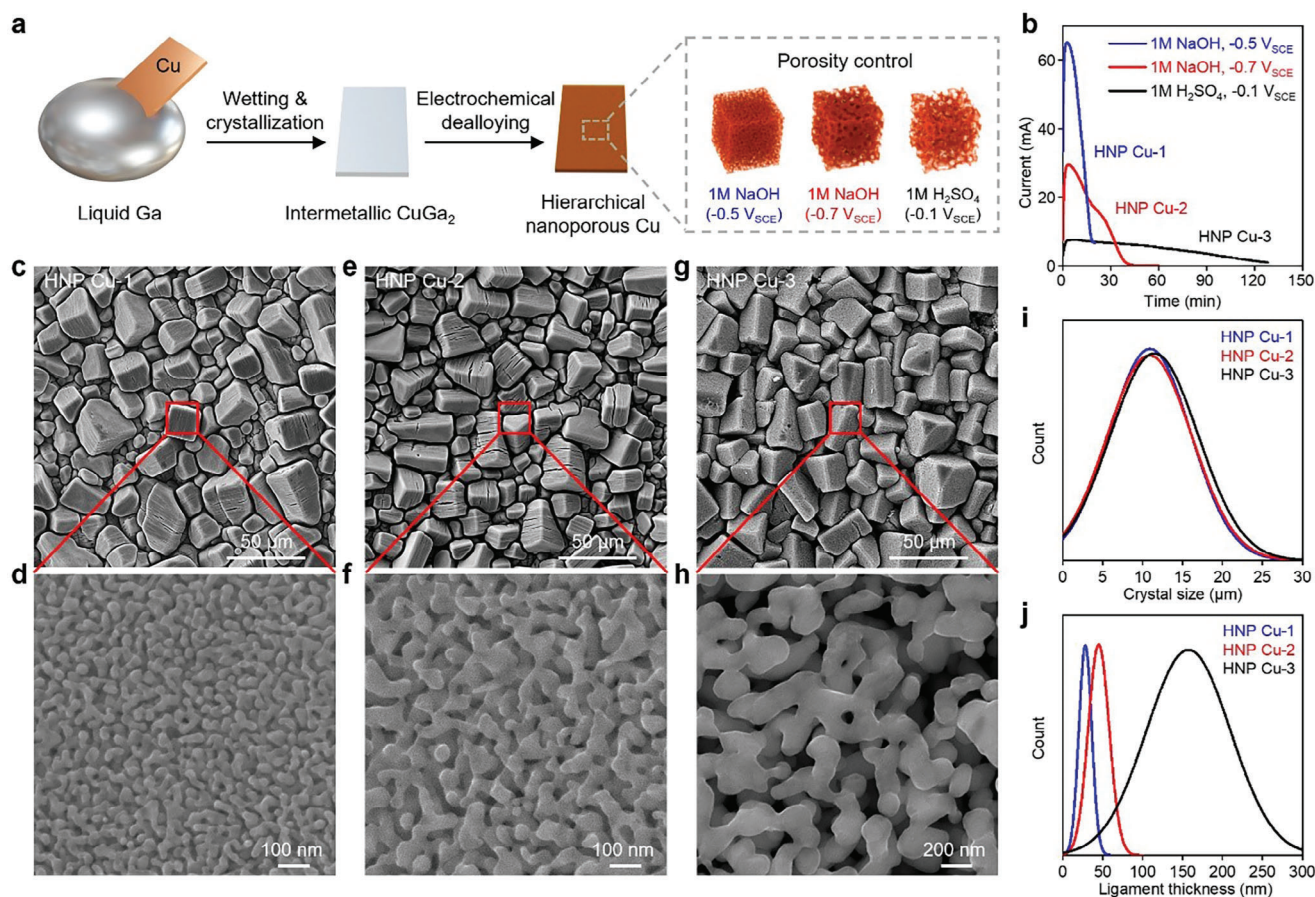


Figure 1. Fabrication of the self-supported HNP Cu catalysts. a) Schematic illustration of the liquid metal-based strategy for transforming Cu foils into HNP structures. b) Chronoamperometric curves of the electrochemical dealloying process for HNP Cu fabrication. c–h) SEM images of the HNP Cu-1 (c and d), HNP Cu-2 (e and f), and HNP Cu-3 (g and h) at different magnifications. i) Crystal size distributions of the preserved tetragonal structures. j) Ligament thickness distributions of the samples.

Table 1. Structural parameters of the HNP Cu catalysts.

Sample name	Crystal size [μm]	Ligament size [nm]	Crystallite size [nm]
HNP Cu-1	10.9	28	16.4
HNP Cu-2	10.8	45	22.8
HNP Cu-3	11.5	157	30.5

are measured to reflect the porosity in this work. Dealloying the CuGa_2 crystals at $-0.7 V_{\text{SCE}}$ to $-0.5 V_{\text{SCE}}$ in a 1 M NaOH solution produces ligaments featuring average sizes of 28 and 45 nm (referred to as HNP Cu-1 and HNP Cu-2 in this paper), respectively (Table 1). Switching the solution from 1 M NaOH to 1 M H_2SO_4 leads to larger ligament (pore) sizes. Ligaments with an average size >150 nm (referred to as HNP Cu-3 in this paper) are obtained under $-0.1 V_{\text{SCE}}$ dealloying potential in 1 M H_2SO_4 solution, (Figure 1c–j; Figure S3, Supporting Information). The dealloying potentials used in this work were determined based on the cyclic voltammetry (CV) curves measured in each solution (Figure S4, Supporting Information).

According to the current understanding of the dealloying process, when Ga is removed from the CuGa_2 crystals, the remain-

ing Cu experiences reconstruction and surface diffusion to create the nanoporous structures. It should be noted that the initial tetragonal shapes of the CuGa_2 crystals are maintained after Ga being removed (Figure 1c–i). Microscale wrinkles are observed on the surface of the samples prepared in NaOH solutions (HNP Cu-1 and HNP Cu-2), presumably due to anisotropic etching in the NaOH at different crystal planes of CuGa_2 . The creation of nanoporous structures leads to changes in the appearance of the samples. UV-vis spectroscopy measurements show that the optical absorbance of the materials increases, and a smaller ligament size results in a stronger absorption of visible light, causing such a change in sample appearance (Figure S5, Supporting Information).

To examine the interior structure of the HNP Cu catalysts, the focused ion beam (FIB) technique is utilized to fabricate thin cross-sectional lamellae by cutting through the nanoporous tetragons (insets of Figure 2a–c). The transmission electron microscopy (TEM) images of the lamellae reveal that dealloying created nanoporous structures throughout the crystals (Figure 2a–c). Different extent of alignment of the nano ligaments is observed in the interior of the HNP Cu-1 and HNP Cu-2 samples but not in the HNP Cu-3 sample. Such ligament

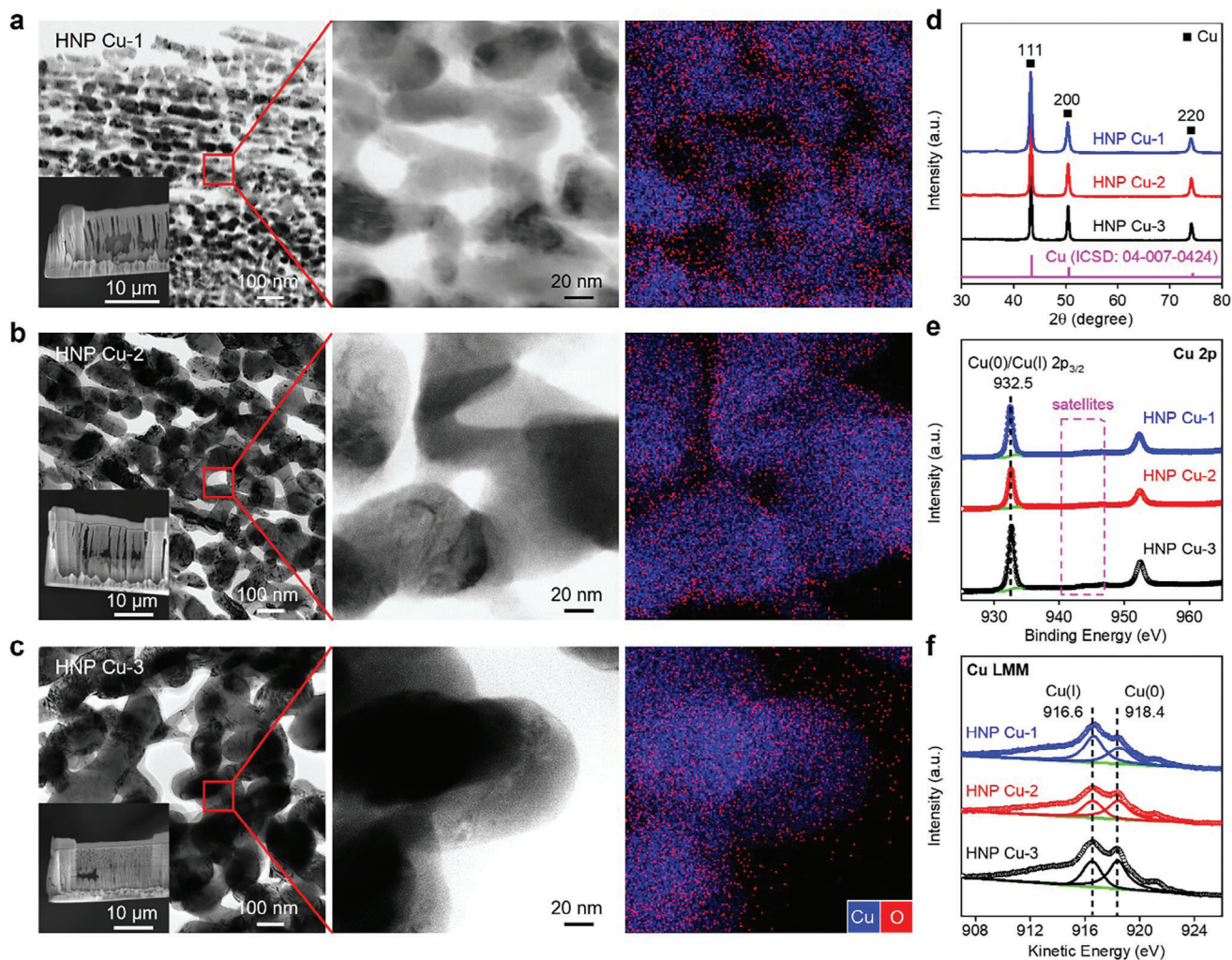


Figure 2. a–c) Interior porous structure of the three HNP Cu samples. TEM images and EDX mappings of the cross-sectional nanoporous Cu lamellae of (a) HNP Cu-1, b) HNP Cu-2, and c) HNP Cu-3. These lamellae (insets) were obtained by cutting through the dealloyed nanoporous Cu samples using the FIB technique. d) XRD patterns of the three HNP Cu samples. e) Cu 2p and (f) Cu LMM XPS spectra showing the presence of Cu (I) and Cu (0) species on the surface of the HNP Cu samples.

alignment is an indication of anisotropic etching of the HNP Cu-1 and HNP Cu-2 samples, which matches our scanning electron microscopy (SEM) observation of wrinkles on the surface of these two samples.

The complete dealloying of the CuGa_2 phase and the effective removal of Ga is evidenced by the absence of CuGa_2 peaks in the X-ray diffraction (XRD) patterns. Compared with the pristine Cu foil which only exhibits a single peak at the $2\theta = 50.46^\circ$ that is indicative of the Cu (200) plane (Figure S6, Supporting Information), all the three HNP Cu samples show highly polycrystalline structures featuring three low index planes, namely the (111), (200) and (220) planes (Figure 2d), of metallic copper. This result implies that the liquid-metal-assisted approach is able to transform monocrystalline Cu into polycrystalline Cu with intensified exposed grains and grain boundaries. Ga removal is also confirmed through the energy-dispersive X-ray (EDX) spectra collected by both the SEM and TEM techniques (Figures S7 and S8, Supporting Information). The Scherrer equation based

on the full width at half maximum (FWHM) of the most prominent (111) XRD peak is used to estimate the size of the crystallites, which form the ligament structures (Table 1). The result suggests that the nano ligaments of the three HNP Cu samples are built up by crystallites with characteristic sizes of 16.4 nm for HNP Cu-1 (average ligament size 28 nm), 22.8 nm for HNP Cu-2 (average ligament size 45 nm), and 30.5 nm for HNP Cu-3 (average ligament size 157 nm). Furthermore, the specific surface area of the three HNP Cu was determined through Brunauer–Emmett–Teller (BET) method. The N_2 adsorption/desorption isotherms of the three HNP Cu catalysts at 77 K are exhibited in Figure S9 (Supporting Information). A hysteresis loop was discerned in the isotherm of HNP Cu-1, caused by capillary condensation in mesopores. In contrast, no hysteresis loop was observed in the isotherms of HNP Cu-2 and HNP Cu-3, indicating the predominance of macropores. As shown in Figure S10 (Supporting Information), HNP Cu-2 has the largest specific surface area at $59.7 \text{ m}^2 \text{ g}^{-1}$, followed by

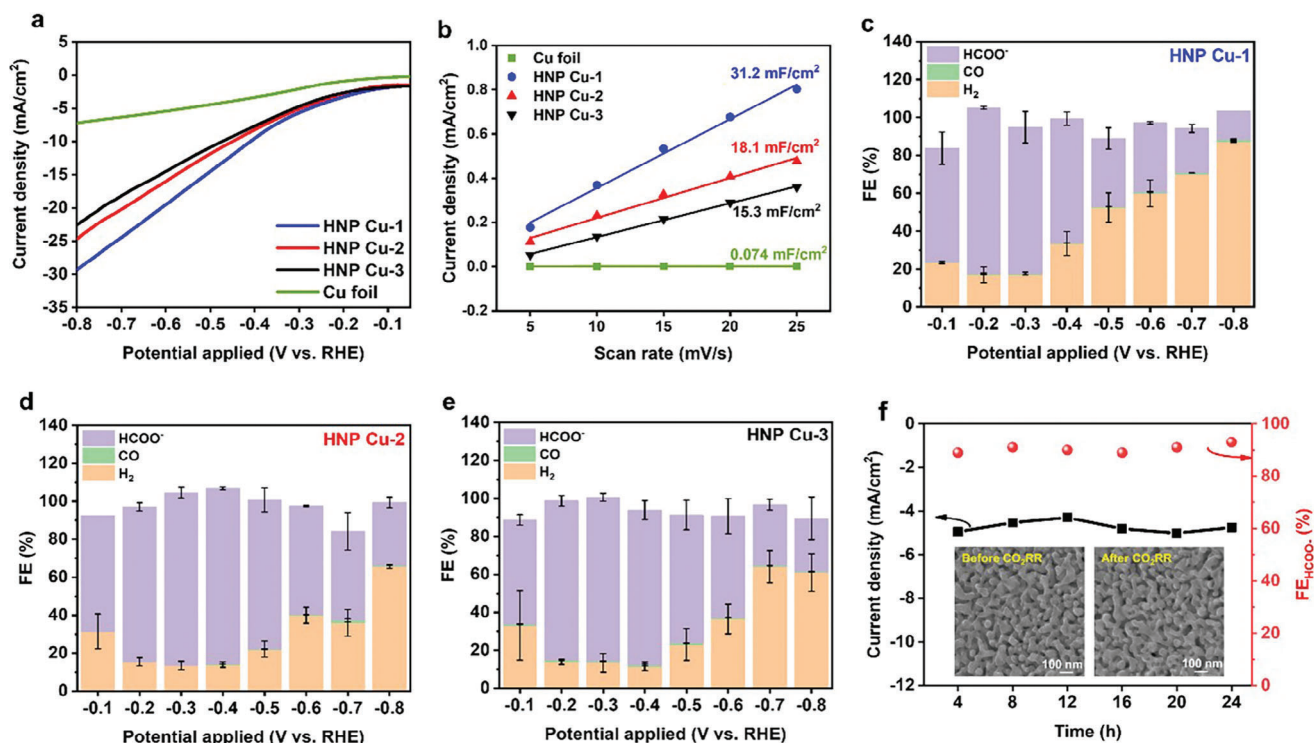


Figure 3. a) LSV curves of three HNP Cu and Cu foil in CO_2 -saturated 0.1 M $\text{KHCO}_3 + 0.15$ mM CTAB aqueous solution. b) The double-layer capacitance (C_{dl}) of Cu foil and three HNP Cu catalysts (scan rate: 5, 10, 15, 20, 25 mV s^{-1}). c–e) CO_2RR performance of HNP Cu-1 (28 nm), HNP Cu-2 (45 nm) and HNP Cu-3 (157 nm), respectively. f) Stability test of HNP Cu-2 across 24-h continuous CO_2 electrolysis at -0.3 V_{RHE} (inset: SEM images of the HNP Cu-2 before and after CO_2 electrolysis).

HNP Cu-1 and HNP Cu-3, measuring 43.8 and 32.4 $\text{m}^2 \text{g}^{-1}$, respectively.

TEM EDX element mappings suggest the formation of a thin oxide layer on the surface of the Cu nano ligaments of the as-prepared (dealloyed) samples. X-ray photoelectron spectra (XPS) surface analysis of Cu 2p (Figure 2e) and Cu LMM Auger spectra (Figure 2f) reveal that the oxide phase covering the metallic Cu is Cu_2O in the as-prepared samples. The absence of the Cu^{2+} satellites in the Cu 2p spectra rules out the existence of CuO (Figure 2e). This is further supported by the strong O 1s peak at 530.56 eV, which is suggestive of the lattice O in the Cu_2O matrix (Figure S11, Supporting Information).^[22] Our comprehensive analyses show that the HNP Cu samples consist of polycrystalline metallic Cu which is slightly oxidized to Cu_2O on the surface of the nano ligaments. The three samples share similar chemical compositions, with their primary distinctions residing in their ligament (pore) size and crystallite size. These differences allow for the examination of how they influence the performance of CO_2RR .

2.2. Electrocatalytic CO_2 Reduction Performance

CO_2 electrolysis is undertaken in a gas-tight two-compartment electrochemical cell to investigate the CO_2RR performance of the HNP Cu catalysts. CO_2 -saturated 0.1 M KHCO_3 aqueous solution with CTAB additive (0.15 mM) is employed as the electrolyte. Linear sweep voltammetry (LSV) curves of the HNP Cu

and pristine Cu foil are first recorded. As shown in Figure 3a, all the three HNP Cu catalysts exhibit lower onset potential and higher current density under the same applied potentials compared to the pristine Cu foil, indicating the higher electrochemical activity of the HNP Cu catalysts. Among the three types of HNP Cu catalysts evaluated, HNP Cu-1 demonstrated the highest overall current density, attributed to its smallest crystallite and ligament sizes. Conversely, HNP Cu-2 and HNP Cu-3, which feature larger ligament sizes, exhibited lower current densities. The ECSA of the HNP Cu catalysts and pristine Cu foil are then determined by measuring the double-layer capacitance (C_{dl}) in the non-Faradaic region (Figure S12, Supporting Information). As depicted in Figure 3b, HNP Cu-1 exhibited the highest C_{dl} with 31.2 mF cm^{-2} , followed by HNP Cu-2 with 18.1 mF cm^{-2} , and HNP Cu-3 with 15.3 mF cm^{-2} , and the ECSA calculated based on the C_{dl} values are 268.97 cm^2 for HNP Cu-1, 156.04 cm^2 for HNP Cu-2, 131.82 cm^2 for HNP Cu-3, respectively. The observed trend in ECSA changes aligns closely with the variations in overall current density measured for the three HNP Cu catalysts. Notably, the ECSA of all HNP Cu catalysts is found to be hundreds of times greater than that of the Cu foil, a significant increase attributed to the enlarged ECSA provided by the hierarchical nanoporous structure. Additionally, there is an evident difference between the LSV curves of respectively recorded in CO_2 - and N_2 -saturated electrolytes for all the HNP Cu catalysts (Figure S13, Supporting Information), whereas the increased current density in the presence of CO_2 is attributed by the occurrence of CO_2RR alongside the hydrogen evolution reaction (HER).

The CO₂RR performance of the HNP Cu catalysts are then evaluated across same potential window. As shown in Figure 3c–e, all three HNP Cu can initiate the CO₂RR at a relatively low potential of $-0.1 V_{\text{RHE}}$, with the Faradaic efficiency of formate (FE_{formate}) being 60%, 61%, and 55% for HNP Cu-1, HNP Cu-2, and HNP Cu-3, respectively. This contrasts with the performance of Cu foil, where formate production only begins at a more negative potential of $-0.5 V_{\text{RHE}}$, achieving a maximum FE_{formate} of merely 40% with the majority of other products being H₂ (Figure S14, Supporting Information). This clearly demonstrates the superior CO₂RR activity of the HNP Cu catalysts over HER, highlighting the advantages of their hierarchical nanoporous structure in exposing a larger active surface area.^[23] The FE_{formate} obtained from HNP Cu-1 peaks at 87.5% under $-0.2 V_{\text{RHE}}$, however, a significant drop in CO₂RR activity is observed beyond this point, with H₂ progressively emerging as the predominant product. HNP Cu-2 (with a ligament size of 45 nm) demonstrates a higher selectivity toward formate at both $-0.3 V_{\text{RHE}}$ ($FE_{\text{formate}} = 91\%$) and $-0.4 V_{\text{RHE}}$ ($FE_{\text{formate}} = 92.5\%$). HNP Cu-3, featuring a ligament size of 157 nm, achieves its peak CO₂RR performance with a FE_{formate} of 86.5% at $-0.3 V_{\text{RHE}}$. It is worth noting that both HNP Cu-2 and HNP Cu-3 show more effective inhibition of HER under most of the potentials tested, especially when the applied potential goes more negative. Overall, HNP Cu-2 and HNP Cu-3 exhibit similar CO₂RR performance by evaluating FE_{formate} and H₂ inhibition comprehensively, and HNP Cu-2 catalyst is selected for the following investigation owing to its higher current density and peak FE_{formate} . To ensure the formate production is not a result of CTAB decomposition or other chemical reactions, nuclear magnetic resonance (NMR) spectroscopy of the electrolyte before and after CO₂ electrolysis on HNP Cu-2 is recorded, respectively. As shown in Figure S15 (Supporting Information), the peak indicating the H atom in formate (HCOO⁻) is the only newly generated peak after CO₂ electrolysis. Meanwhile, there is no change regarding all the peaks attributed by CTAB,^[24] excluding the possibility that the generated HCOO⁻ comes from the chemical reactions associated with CTAB.

The long-term stability of the HNP Cu-2 catalyst has been evaluated during a 24-h session of CO₂RR at $-0.3 V_{\text{RHE}}$, revealing that both the current density ($\approx 4.7 \text{ mA cm}^{-2}$) as well as the FE_{formate} (averagely 92%) remains virtually unchanged throughout the testing period (Figure 3f), and no discernible changes are observed in the morphology of HNP Cu-2 before and after CO₂RR, as confirmed by SEM (inset of Figure 3f). The performance of HNP Cu-2 is arguably the highest for electrochemical CO₂-to-formate conversion among single-component Cu catalysts under ambient conditions at a mild potential (Table S1, Supporting Information). Moreover, our fabrication method for the HNP Cu is cost-effective owing to the following facts: commercially available Cu foils are used as the starting material, the majority of the Ga solvent is reused, and the ionized Ga produced during dealloying can be reduced/recycled (e.g., electrochemical reduction) for large-scale fabrication. In addition, the processing temperature is low during intermetallic phase formation, and the processing solutions involved in the dealloying treatment are commonly used acidic (H₂SO₄) and basic (NaOH) solutions, which makes our fabrication strategy more energetically efficient and sustainable than other fabrication methods.

It is well-acknowledged that Cu species undergo oxidation easily under an ambient environment, although a pre-reduction process is conducted prior to the CO₂RR, the complete elimination of oxidized Cu species cannot be guaranteed due to the highly hierarchical structure. Therefore, in-situ X-ray adsorption spectroscopy (in-situ XAS) measurements are performed to track any change in the chemical state or coordination environment of the Cu during the CO₂ electrocatalysis. A customized in-situ XAS cell (Figure S16a, Supporting Information) is employed for the measurements. X-ray adsorption near-edge structure (XANES) and extended X-ray adsorption fine structure (EXAFS) are conducted at Cu K-edge to track any change in the chemical state or coordination environment of Cu species in HNP Cu-2 under real operating conditions of CO₂RR. In-situ XANES spectra are recorded for HNP Cu-2 before, during (potential of -0.2 , -0.3 , and $-0.5 V_{\text{RHE}}$ have been applied for CO₂ electrolysis, respectively) and after CO₂RR process. As depicted in Figure S16b (Supporting Information), the HNP Cu-2 shows the same adsorption edge as the standard Cu foil reference before a negative potential is applied, confirming that the oxidized Cu species have been completely reduced to metallic Cu in the pre-reduction process. With a negative potential being applied and further reduced for commencing CO₂ reduction, the HNP Cu-2 consistently shows similar adsorption edge with Cu foil reference, confirming the valence state of Cu stays as Cu⁰ during the CO₂-to-formate conversion. Upon stopping applying any potential, there is no immediate generation of any oxidized Cu species. Besides, no distinguishable changes have been observed from the EXAFS spectra (Figure S16c, Supporting Information), where Cu-Cu is the only bonding exists across the in-situ tests, implying there is no change in the coordination environment of Cu in HNP Cu-2 throughout the CO₂RR process.

The different CO₂RR performances obtained on the HNP Cu catalysts can be connected to the difference in their crystallite size and nanoporous network. Previous research has conclusively shown that size effect is of great significance for CO₂RR activity,^[23,25] with HER preferentially occurring on the surfaces of smaller nanoparticles.^[26] Among the three HNP Cu catalysts, HNP Cu-1 has the smallest crystallite sizes, featuring surfaces of small-diameter nanocrystals enriched with characteristics such as higher density of edge sites, corner sites and undercoordinated surfaces that promote HER.^[27] Size impact is much alleviated on HNP Cu-2 and HNP Cu-3 which are assembled by larger crystallites, which therefore leads to obvious HER inhibition on these two catalysts. The differences in the intrinsic CO₂RR activities of the three HNP Cu are further investigated. First, electrochemical impedance spectroscopy (EIS) is measured to study the charge transfer resistance of the HNP Cu catalysts. As shown in Figure S17 (Supporting Information), all the three HNP Cu show similar R_s , which accounts for the sheet resistance of the reaction system. The charge transfer resistance (R_{ct}) of the three HNP Cu is in a descending order of HNP Cu-1 > HNP Cu-2 > HNP Cu-3, which is in good accordance with both the LSV measurements and ECSA results, demonstrating that the larger surface area contributes to more accelerated charge transfer over the HNP Cu surfaces. However, after normalized by the ECSA, HNP Cu-1 is found to show the lowest formate partial current density ($j_{\text{formate}}^{\text{-ECSA}}$) among all the HNP Cu catalysts (Figure 4a), suggesting that the effect of ECSA is not the only

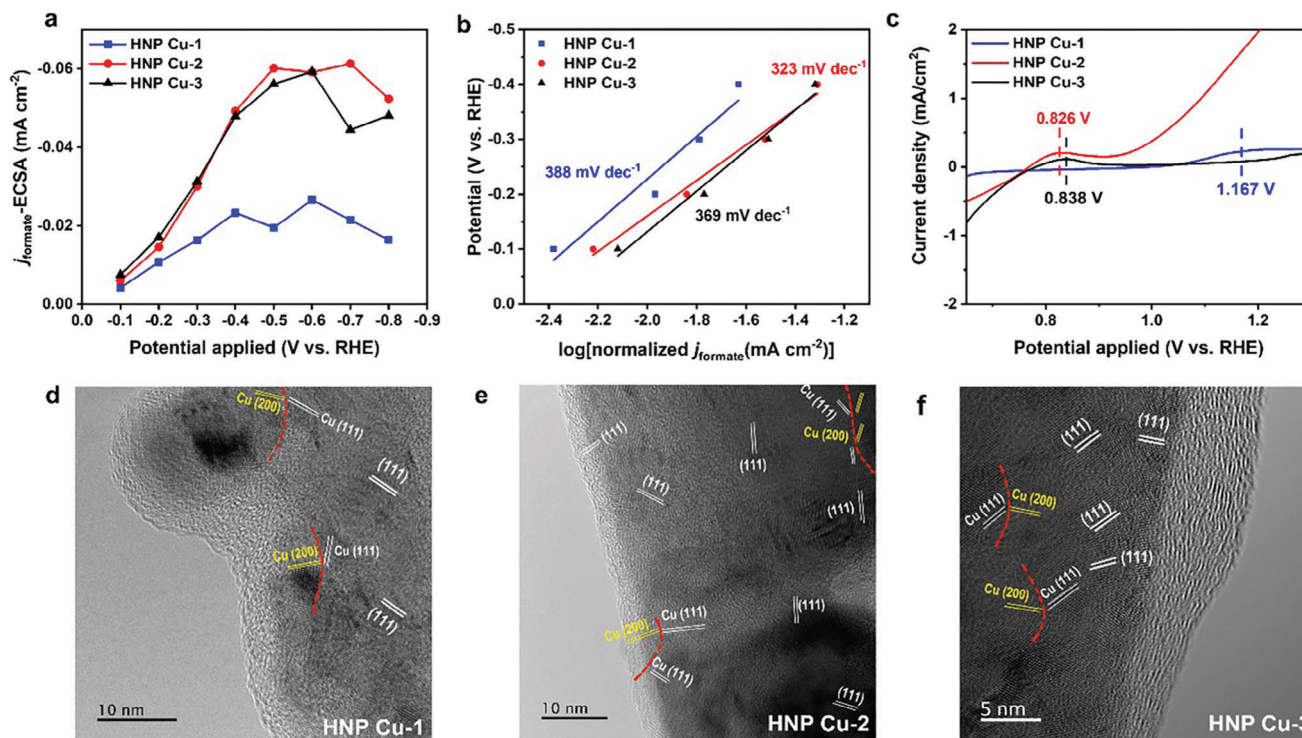


Figure 4. a) ECSA-normalized formate partial current density on the three HNP Cu catalysts. b) Tafel slope calculated by ECSA-normalized formate partial current density ($j_{\text{formate}}\text{-ECSA}$). c) Single oxidative LSV curves in N_2 -saturated 0.1 M NaOH aqueous solution of the three HNP Cu catalysts. d–f) HRTEM images with the identification of Cu (111) facets and grain boundaries of HNP Cu-1, HNP Cu-2, and HNP Cu-3, respectively.

contributor to the enhanced CO_2 RR performance.^[28] HNP Cu-2 and HNP Cu-3 show similar $j_{\text{formate}}\text{-ECSA}$ value in the lower potential range and start to show differences when the potential goes more negative, and nevertheless are much higher than the HNP Cu-1, implying higher intrinsic activity of these two catalysts.

Tafel slope is then calculated based on the $j_{\text{formate}}\text{-ECSA}$ values to gain more insights in the kinetics on the HNP Cu. As displayed in Figure 4b, the Tafel slope of the HNP Cu-2 and HNP Cu-3 are smaller than the HNP Cu-1, demonstrating accelerated kinetics for CO_2 RR on HNP Cu with larger ligament sizes. Besides, all the three HNP Cu show Tafel slope values that are greater than 120 mV dec^{-1} , indicating that the rate-determining step of CO_2 conversion on the HNP Cu is the CO_2 activation step: $\text{CO}_2 \rightarrow * \text{CO}_2^-$.^[29] Thereafter, the binding intensity of $* \text{CO}_2^-$ intermediate on the three HNP Cu has been determined by conducting LSV measurement in N_2 -saturated 0.1 M NaOH solution. It has been demonstrated previously that the surface adsorbed OH^- can be used as a surrogate for $* \text{CO}_2^-$ intermediate,^[30] and greater binding intensity of $* \text{CO}_2^-$ takes place at more negative potentials.^[31] As shown in Figure 4c, HNP Cu-2 possesses the strongest adsorption affinity of $* \text{CO}_2^-$ intermediate, therefore could more efficiently stabilize the $* \text{CO}_2^-$ intermediate for the following reaction steps. The adsorption of $* \text{CO}_2^-$ over HNP Cu-3 is anodically shifted by $0.012 \text{ V}_{\text{RHE}}$, indicating weaker $* \text{CO}_2^-$ adsorption on its surface and assumably lower CO_2 RR performance. The OH^- adsorption peak further shifted by $0.341 \text{ V}_{\text{RHE}}$ over HNP Cu-1, implying an even weaker $* \text{CO}_2^-$ binding on HNP Cu with small crystallite/ligament size, which aligns well with its lower CO_2 RR

performance especially when the potential becomes more negative. It has been previously addressed that porous materials with unsuitable pore size have insufficient ability to confine reaction intermediates therefore exhibit lower reactivity.^[32] Overall, the CO_2 RR performance of the three HNP Cu catalysts correlates well with their binding affinity toward $* \text{CO}_2^-$, demonstrating the efficiency of our synthesize approach in obtaining controllable nanostructure with desired confinement of reaction intermediates.

We proceeded to investigate the CO_2 reduction pathway on the HNP Cu-2 catalyst by recording in-situ synchrotron-sourced Fourier Transform Infrared spectrum (in-situ SR-FTIR) during the CO_2 RR process. A customized in-situ FTIR cell as shown in Figure S18a (Supporting Information) is employed for the measurements. As shown in Figure S18b (Supporting Information), a positive peak (indicating generated species) at $\approx 1250 \text{ cm}^{-1}$ starts to merge when a negative potential is applied, which is attributed to the generation of the $* \text{CO}_2^-$ intermediate,^[33] indicating the activation step of the CO_2 molecule on the surface of the HNP Cu. The negative band (indicating consumed species) centres at 1600 cm^{-1} which is assigned to H_2O ^[34] is getting more obvious as the potential becoming more negative, refers to the progression of H_2O consumption. Simultaneously, a positive peak at 1380 cm^{-1} starts to merge when a negative potential is being applied and shows increased intensity when the potential is further reduced, which is dedicated by the generation of the key intermediate $* \text{OCHO}$.^[35] These results confirmed that the formation pathway of formate on the HNP Cu catalyst as follows: $\text{CO}_2 \rightarrow * \text{CO}_2^- \rightarrow * \text{OCHO} \rightarrow * \text{HCOOH} \rightarrow \text{HCOOH}$.

It has been intensively reported that CO₂RR product distribution on Cu-based electrocatalysts exhibits facet-dependent catalytic behaviours.^[36] The energetically favoured formate formation over other CO₂RR products on Cu (111) facet have been well-acknowledged in previous experimental and calculation studies.^[37] As suggested in the work of Durand et al.,^[38] the Cu (111) facet has the weakest binding energy of *COOH intermediate (key intermediate for CO formation) therefore the CO production is unfavourable. Lu et al.,^[39] also suggested the preferred formate formation than CO formation over Cu (111) facet as the adsorption energy toward *OCHO only requires minimal energy while the formation of *COOH intermediate is endothermic with high energy requirements. As mentioned earlier, the Cu foil transformed from monocrystalline structure (single crystal featuring only 200 facet) to a polycrystalline structure featuring two newly originated Cu (111) and Cu (200) facets after the dealloying of the CuGa₂ intermetallic crystals. As confirmed by XRD, Cu (111) is the dominant facet in all the three HNP Cu, and high-resolution transmission electronic microscopy (HRTEM) also showed the existence of densely packed Cu (111) facets in all the three HNP Cu (Figure 4d–f). The exposed preferred Cu (111) facets therefore enable a formate-favorable reaction pathway for CO₂RR in the HNP Cu. Moreover, grain boundaries in polycrystalline materials have been well-recognised as beneficial for electrochemical CO₂ conversion, due to the plentiful availability of the grain boundary-supported and stabilized metastable active sites.^[40] As displayed in Figure 4d–f, grain boundaries between Cu (111) and Cu (200) facets have been clearly identified for all the three HNP Cu. Previous experimental studies have shown that the Cu (111)/Cu (200) grain boundary favours CO₂-to-formate conversion over other CO₂RR products.^[41] Furthermore, the research by Luo et al.,^[42] showed that the formation of formate is energetically favoured on stepped Cu surfaces with (111) facets, demonstrating that the surface defects (step, edge, grain boundary) and preferred facets synergistically facilitate the CO₂ reduction reaction process.

3. Conclusion

This study presents a novel liquid metal-assisted approach for fabricating HNP Cu catalysts, which enabled us to tailor the nanoscale porous structures and investigate their influence on electrocatalysis. Three types of polycrystalline HNP Cu with well-defined ligament/pore and crystallite sizes were fabricated at low temperatures during liquid metal alloying (synthesizing CuGa₂) and mild dealloying conditions. The electrocatalytic CO₂ reduction performance of these polycrystalline HNP Cu catalysts is found to be closely linked to their crystallite size and porous architecture. The HNP Cu catalyst with intermediate ligament/pore (45 nm) and crystallite sizes (22.8 nm) demonstrates exceptional efficiency in converting CO₂ to formate, achieving a FE_{formate} of 91% at a relatively low applied potential of $-0.3 V_{RHE}$. This enhanced catalytic performance is attributed to the increased surface area (for increased current density), preferred exposed Cu facets, and abundant grain boundaries (for improving formate selectivity) provided by the nanoporous structure. A potential reaction mechanism involving the *OCHO intermediate has been established by in-situ FTIR spectra. The introduction of liquid metal significantly improves the degree of freedom for structural

control during nanofabrication. This in turn provides an appealing structural design strategy for crafting CO₂RR catalysts with adjustable catalytic activities and narrow product distributions, and thus new perspectives for developing high-performance CO₂ reduction electrocatalysts.

4. Experimental Section

Fabrication of Hierarchical Nanoporous Cu—Preparation of Cu-Ga Intermetallic Crystals: A 30 μm-thick Cu foil (99.99% purity, Xiamen Zopin New Material Limited) was used as the precursory substrate for intermetallic formation. The Cu foil was immersed in hydrochloric acid (HCl, 1 M) for 10 min and then rinsed with deionized (DI) water to eliminate the native oxide layer. The pre-treated Cu foil was then submerged in liquid Ga (99.999% purity, Indium corporation) for 5 min inside an N₂-filled glovebox, allowing the liquid metal Ga to wet and cover the surface of the Cu foil. The Ga-covered Cu foil was then placed on a hot plate and kept at 100 °C for 12 h, allowing the liquid Ga and Cu foil to react and form Cu-Ga intermetallic crystals. The samples were taken out of the glovebox and sonicated in warm absolute ethanol (60 °C) until the remaining liquid Ga on the surface was completely removed, exposing the intermetallic crystals.

Formation of HNP Cu: The HNP Cu was obtained by selectively dissolving Ga from the Cu-Ga intermetallic crystals. A standard three-electrode potentiostat (CHI-650E, CH Instruments, Inc.) was employed, and two types of aqueous solutions (NaOH and H₂SO₄, 1 M) were chosen as the dealloying electrolytes. A saturated calomel electrode (SCE) and a gold wire were used as the reference electrode and the counter electrode, respectively. The Cu-Ga intermetallic samples were used as the working electrode which were dealloyed at constant potentials. The dealloying potential and electrolyte were varied to fine-tune the structural porosity. Three hierarchical nanoporous Cu foils with different ligament (pore) sizes were successfully fabricated (donated as HNP Cu-1, HNP Cu-2, and HNP Cu-3) by the electrochemical dealloying of CuGa₂ intermetallic crystals at room temperature. For the preparation of HNP Cu-1 in a 1 M NaOH solution at $-0.5 V_{SCE}$, the experiment was halted manually at the inflection point of the chronoamperometric curve (after which the dealloying current became small and stabilized) to prevent oxidation of Cu. For the preparation of HNP Cu-2, the dealloying process was conducted in a 1 M NaOH solution at $-0.7 V_{SCE}$, which continued until the current became negligible (0.05 mA). When fabricating the HNP Cu-3, the dealloying was processed in a 1 M H₂SO₄ solution at $-0.1 V_{SCE}$ till the dealloying current dropped to 1 mA (further dealloying in H₂SO₄ can compromise the structural integrity), and followed by a second dealloying step in NaOH at $-0.7 V_{SCE}$ till the current reached 0.05 mA. The samples were washed thoroughly in DI water to remove any precipitation residuals.

Characterization: The cyclic voltammetry (CV, scan rate 50 mV s⁻¹), and chronoamperometric curves for the preparation of the HNP Cu samples were measured using the CHI-650E potentiostat. The morphologies of the HNP Cu samples were investigated employing a JEOL JSM-IT500 field-emission scanning electron microscopy (SEM) system. The transmission electron microscopy (TEM) images, energy-dispersive X-ray (EDX) spectra, and mappings of the lamellae were acquired utilizing a JEOL JEM-F200 TEM system. The HNP Cu sample was cut using a Thermo Fisher Helios G4 plasma focused ion beam (FIB) with Xe ion source and an interior nanoporous Cu lamellae was taken out for TEM imaging and EDX mapping. The ultraviolet-visible (UV-vis) absorption spectra were collected with an Agilent Cary5000 UV-vis spectrometer with zero/baseline correction. The X-ray diffraction (XRD) patterns were obtained using an MPD Xpert multipurpose XRD system. It should be noted that the nanoporous Cu layer was peeled off and used for XRD analysis in order to eliminate the XRD signal from the supporting Cu beneath the nanoporous structures. The X-ray photoelectron spectra (XPS) was recorded on Thermo ESCALAB250i and the binding energy was corrected by the C_{1s} peak of 284.8 eV. The specific surface area of the three HNP Cu catalysts was determined through the Brunauer–Emmett–Teller (BET)

method using a NOVAtouch LX2 BET surface area analyzer. The HNP Cu samples were degassed under vacuum at 120 °C for 8 h prior to the N₂ adsorption/desorption experiment at a temperature of 77 K. The nanoporous Cu layer was peeled off and utilized for BET measurement, eliminating the influence of the supporting non-porous Cu beneath.

Electrocatalytic CO₂ Reduction Performance Test: The as-prepared HNP Cu is freestanding and thus can be directly used as the working electrode without further treatment. The working area of the HNP Cu electrode is fixed at 0.25 cm². Ag/AgCl (filled with saturated KCl) and Pt foil were used as the reference and counter electrodes, respectively. All potentials were converted to reversible hydrogen electrode (RHE) with the equation of E (vs RHE) = E (Ag/AgCl) + 0.059*pH + 0.197 V. All the electrochemical tests were conducted without iR compensation. Linear sweep voltammetry (LSV) curves were recorded at the scan rate of 5 mV s⁻¹. Electrochemical impedance spectroscopy (EIS) was implemented in the frequency range of 10⁶-0.1 Hz at -0.3 V_{RHE} for the three HNP Cu. The electrocatalytic CO₂ reduction performances of the three HNP Cu catalysts and the pristine Cu foil were measured in a typical H-type cell in 0.1 M KHCO₃ aqueous solution with the addition of 0.15 mM cetyltrimethylammonium bromide (CTAB), whereas CO₂ was constantly purged into the electrolyte for at least 30 min before each electrolysis. Pre-reduction was conducted on all the samples in CO₂RR environment prior to the CO₂ electrolysis to eliminate the effect of any oxidized Cu species. Each error bar was obtained by two independent electrochemical measurements. The gas products were analyzed by gas chromatography (GC-2010, Shimadzu) and the liquid products were analyzed by nuclear magnetic resonance (600 MHz Avance III NMR, Bruker). The quantified product amount was then used for the corresponding FE calculation through the following Equation (1):

$$FE (\%) = \frac{z \cdot n \cdot F}{Q} * 100 \quad (1)$$

where, z represents the number of electrons required to produce a specific product (eg. z = 2 for H₂, CO, and formate); n represents the molar amount of the product calculated based on GC or NMR quantification; F is the Faraday constant (96 485 C mol⁻¹); Q represents the total charge consumed during the CO₂RR process. To determine the electrochemical active surface area (ECSA), the cyclic voltammetry (CV) curves of all three HNP Cu and Cu foil were recorded in non-faradaic region (0.22 – 0.32 V_{RHE}) at different scan rates (5, 10, 15, 20, and 25 mV s⁻¹, respectively), and the current densities at 0.27 V_{RHE} were used to calculate the double-layer capacitance through the following Equation (2):

$$C_{dl} = \frac{(j_a - j_c)}{2} \quad (2)$$

where, j_a and j_c is the anode and cathode current density obtained at 0.27 V_{RHE}, respectively. As known, ECSA and C_{dl} is in linear correlation according to the following Equation (3):

$$ECSA = R_f * S = \frac{C_{dl}}{C_s} * S \quad (3)$$

where, R_f is the roughness factor, S is the geometric area of the working electrode (in this work S = 0.25 cm²), C_s is the double-layer capacitance per unit area with reference to a smooth metal foil, of which the value is 29 μF.^[43]

Synchrotron-Sourced XAS and FTIR Microspectroscopy: In-situ X-ray adsorption spectrum (in situ XAS) was recorded at the XAS beamline (Australian Synchrotron) using a self-designed in-situ cell equipped with an Ag/AgCl as the reference electrode and a Pt wire as the counter electrode, respectively. In-situ synchrotron-sourced Fourier Transform Infrared spectrum (in-situ SR-FTIR) spectral data was recorded at the IRM beamline (Australian Synchrotron) using a customized in-situ FTIR cell with 0.5-mm-thick ZnSe top window in reflectance mode. The IRM beamline was equipped with a Bruker Vertex 80v spectrometer coupled with a Hyperion 3000 FTIR microscope and a liquid nitrogen-cooled narrow-band mercury

cadmium telluride (MCT) detector (Bruker Optik GmbH, Ettlingen, Germany). All the SR-FTIR spectra were recorded within a spectral range of 3800–700 cm⁻¹ using 4 cm⁻¹ spectral resolution. Blackman-Harris 3-Term apodization, Mertz phase correction, and zero-filling factor of 2 were set as default acquisition parameters using OPUS 8 software suite (Bruker Optik GmbH, Ettlingen, Germany).

Supporting Information

Supporting Information is available from the Wiley Online Library or from the author.

Acknowledgements

This work was supported by the Australian Research Council (ARC ITRP Schemes: IC200100023, IH180100020). X.L. acknowledges the UNSW Scientia Scheme for financial supports. This work was also partially supported by the ARC Discovery Early Career Researcher Award (DE220100816), the ARC Laureate Fellowship Grant (FL180100053), and the ARC Center of Excellence FLEET Grant (CE170100039). The authors acknowledge the facilities and the scientific/technical assistance of Microscopy Australia at the Electron Microscope Unit (EMU), and other characterization facilities within the Mark Wainwright Analytical Centre (MWAC) at UNSW Sydney. The authors acknowledge the grant (AS233/XAS/20640) for XAS beamtime and the grant (AS2023-1/IRM/19466) for IR beamtime at the Australian Synchrotron.

Open access publishing facilitated by University of New South Wales, as part of the Wiley - University of New South Wales agreement via the Council of Australian University Librarians.

Conflict of Interest

The authors declare no conflict of interest.

Author Contributions

W.Z. and Y.C. contributed equally to this work. W.Z. and Y.C. conceived experiments, conducted data analysis, and wrote the first manuscript. J.T. and X.L. supervised the project and revised the manuscript. R.Y. helped with software and visualization. C.K. helped with the FIB technique. S.Z. and C.H. helped with in situ measurements. J.V. assisted with in situ FTIR data acquisition. G.M., K. K.-Z., and R.A. helped with manuscript reviewing and editing. All authors contributed to the manuscript revision.

Data Availability Statement

The data that support the findings of this study are available from the corresponding author upon reasonable request.

Keywords

electrochemical CO₂ conversion, hierarchical nanoporous copper, liquid metal

Received: June 17, 2024

Revised: July 18, 2024

Published online: July 30, 2024

[1] a) O. Heffernan, *Nat. Clim. Change* **2009**, 1, 109; b) R. Wennersten, Q. Sun, H. Li, J. *Clean Prod.* **2015**, 103, 724.

- [2] a) Z. Ma, U. LeGrand, E. Pahija, J. R. Tavares, D. C. Boffito, *Ind. Eng. Chem. Res.* **2021**, *60*, 803; b) B. Thijs, J. Rongé, J. A. Martens, *Green Chem.* **2022**, *24*, 2287.
- [3] a) M. Alvarez-Guerra, S. Quintanilla, A. Irbien, *Chem. Eng. J.* **2012**, *207–208*, 278; b) M. D. Porosoff, X. Yang, J. A. Boscoboinik, J. G. Chen, *Angew. Chem., Int. Ed.* **2014**, *53*, 6705.
- [4] Z. Yang, F. E. Oropeza, K. H. L. Zhang, *APL Mater.* **2020**, *8*, 060901.
- [5] N. Han, Y. Wang, H. Yang, J. Deng, J. Wu, Y. Li, Y. Li, *Nat. Commun.* **2018**, *9*, 1320.
- [6] P. Li, F. Yang, J. Li, Q. Zhu, J. W. Xu, X. J. Loh, K.-W. Huang, W. Hu, J. Lu, *Adv. Energy Mater.* **2023**, *13*, 2301597.
- [7] Z. Chen, H. Yang, Z. Kang, M. Driess, P. W. Menezes, *Adv. Mater.* **2022**, *34*, 2108432.
- [8] a) Y. Hori, K. Kikuchi, A. Murata, S. Suzuki, *Chem. Lett.* **1986**, *15*, 897; b) Y. Hori, A. Murata, R. Takahashi, *J. Chem. Soc., Faraday Trans. 1* **1989**, *85*, 2309; c) K. P. Kuhl, E. R. Cave, D. N. Abram, T. F. Jaramillo, *Energy Environ. Sci.* **2012**, *5*, 7050.
- [9] L. Peng, Y. Wang, Y. Wang, N. Xu, W. Lou, P. Liu, D. Cai, H. Huang, J. Qiao, *Appl. Catal., B* **2021**, *288*, 120003.
- [10] X. Ma, Y. Zhang, T. Fan, D. Wei, Z. Huang, Z. Zhang, Z. Zhang, Y. Dong, Q. Hong, Z. Chen, X. Yi, *Adv. Funct. Mater.* **2023**, *33*, 2213145.
- [11] a) Z. Gu, H. Shen, L. Shang, X. Lv, L. Qian, G. Zheng, *Small Methods* **2018**, *2*, 1800121; b) Y. Li, F. Cui, M. B. Ross, D. Kim, Y. Sun, P. Yang, *Nano Lett.* **2017**, *17*, 1312; c) A. Thevenon, A. Rosas-Hernández, J. C. Peters, T. Agapie, *Angew. Chem., Int. Ed.* **2019**, *58*, 16952.
- [12] M. Rahaman, A. Dutta, A. Zanetti, P. Broekmann, *ACS Catal.* **2017**, *7*, 7946.
- [13] C. Reller, R. Krause, E. Volkova, B. Schmid, S. Neubauer, A. Rucki, M. Schuster, G. Schmid, *Adv. Energy Mater.* **2017**, *7*, 1602114.
- [14] M. Ma, K. Djanashvili, W. A. Smith, *Angew. Chem., Int. Ed.* **2016**, *55*, 6680.
- [15] S. Sen, D. Liu, G. T. R. Palmore, *ACS Catal.* **2014**, *4*, 3091.
- [16] Z. Lu, C. Li, J. Han, F. Zhang, P. Liu, H. Wang, Z. Wang, C. Cheng, L. Chen, A. Hirata, T. Fujita, J. Erlebacher, M. Chen, *Nat. Commun.* **2018**, *9*, 276.
- [17] a) I. McCue, S. Ryan, K. Hemker, X. Xu, N. Li, M. Chen, J. Erlebacher, *Adv. Energy Mater.* **2016**, *18*, 46; b) P.-A. Geslin, I. McCue, B. Gaskey, J. Erlebacher, A. Karma, *Nat. Commun.* **2015**, *6*, 8887.
- [18] a) Z. Xing, G. Zhang, J. Gao, J. Ye, Z. Zhou, B. Liu, X. Yan, X. Chen, M. Guo, K. Yue, X. Li, Q. Wang, J. Liu, *Adv. Mater.* **2024**, *36*, 2309999; b) Y. Hou, F. Wang, C. Qin, S. Wu, M. Cao, P. Yang, L. Huang, Y. Wu, *Nat. Commun.* **2022**, *13*, 7625.
- [19] a) T. Daeneke, K. Khoshmanesh, N. Mahmood, I. A. de Castro, D. Esrafilzadeh, S. J. Barrow, M. D. Dickey, K. Kalantar-zadeh, *Chem. Soc. Rev.* **2018**, *47*, 4073; b) S. A. Idrus-Saidi, J. Tang, S. Lambie, J. Han, M. Mayyas, M. B. Ghasemian, F.-M. Alliou, S. Cai, P. Koshy, P. Mostaghimi, K. G. Steenbergen, A. S. Barnard, T. Daeneke, N. Gaston, K. Kalantar-Zadeh, *Science* **2022**, *378*, 1118.
- [20] Y. Chi, P. V. Kumar, J. Zheng, C. Kong, R. Yu, L. Johnston, M. B. Ghasemian, M. A. Rahim, T. Kumeria, D. Chu, X. Lu, G. Mao, K. Kalantar-Zadeh, J. Tang, *ACS Nano* **2023**, *17*, 17070.
- [21] a) A. M. Hodge, J. R. Hayes, J. A. Caro, J. Biener, A. V. Hamza, *Adv. Eng. Mater.* **2006**, *8*, 853; b) N. A. Senior, R. C. Newman, *Nanotechnology* **2006**, *17*, 2311.
- [22] a) Y. Chang, B. Shao, J. Wang, F. Chen, W. Zhai, *Adv. Mater. Technol.* **2022**, *7*, 2200293; b) T. Zhao, A. Munis, M. Zheng, J. Hu, H. Teng, L. Wei, *J. Mol. Liq.* **2020**, *316*, 113927.
- [23] Z. Li, D. He, X. Yan, S. Dai, S. Younan, Z. Ke, X. Pan, X. Xiao, H. Wu, J. Gu, *Angew. Chem., Int. Ed.* **2020**, *59*, 18572.
- [24] V. Patel, N. Dharaiya, D. Ray, V. K. Aswal, P. Bahadur, *Colloids Surf. Physicochem. Eng. Aspects* **2014**, *455*, 67.
- [25] a) D. Gao, H. Zhou, J. Wang, S. Miao, F. Yang, G. Wang, J. Wang, X. Bao, *J. Am. Chem. Soc.* **2015**, *137*, 4288; b) M. Rahaman, A. Dutta, P. Broekmann, *ChemSusChem* **2017**, *10*, 1733.
- [26] a) R. Reske, H. Mistry, F. Behafarid, B. Roldan Cuenya, P. Strasser, *J. Am. Chem. Soc.* **2014**, *136*, 6978; b) B. C. Marepally, C. Ampelli, C. Genovese, T. Saboo, S. Perathoner, F. M. Wieser, L. Veyre, J. Canivet, E. A. Quadrelli, G. Centi, *ChemSusChem* **2017**, *10*, 4442; c) J. A. Trindell, J. Clausmeyer, R. M. Crooks, *J. Am. Chem. Soc.* **2017**, *139*, 16161.
- [27] a) O. S. Ivanova, F. P. Zamborini, *J. Am. Chem. Soc.* **2010**, *132*, 70; b) W. Zhu, R. Michalsky, O. n. Metin, H. Lv, S. Guo, C. J. Wright, X. Sun, A. A. Peterson, S. Sun, *J. Am. Chem. Soc.* **2013**, *135*, 16833.
- [28] X. Zhang, X. Sun, S.-X. Guo, A. M. Bond, J. Zhang, *Energy Environ. Sci.* **2019**, *12*, 1334.
- [29] C. W. Lee, N. H. Cho, S. W. Im, M. S. Jee, Y. J. Hwang, B. K. Min, K. T. Nam, *J. Mater. Chem. A* **2018**, *6*, 14043.
- [30] a) F. Lei, W. Liu, Y. Sun, J. Xu, K. Liu, L. Liang, T. Yao, B. Pan, S. Wei, Y. Xie, *Nat. Commun.* **2016**, *7*, 12697; b) Z. Li, A. Cao, Q. Zheng, Y. Fu, T. Wang, K. T. Arul, J.-L. Chen, B. Yang, N. M. Adli, L. Lei, C.-L. Dong, J. Xiao, G. Wu, Y. Hou, *Adv. Mater.* **2021**, *33*, 2005113.
- [31] H. Q. Fu, J. Liu, N. M. Bedford, Y. Wang, J. W. Sun, Y. Zou, M. Dong, J. Wright, H. Diao, P. Liu, H. G. Yang, H. Zhao, *Adv. Mater.* **2022**, *34*, 2202854.
- [32] Y. Zhong, X. Kong, Z. Song, Y. Liu, L. Peng, L. Zhang, X. Luo, J. Zeng, Z. Geng, *Nano Lett.* **2022**, *22*, 2554.
- [33] Q. Cheng, M. Huang, L. Xiao, S. Mou, X. Zhao, Y. Xie, G. Jiang, X. Jiang, F. Dong, *ACS Catal.* **2023**, *13*, 4021.
- [34] a) E. P. Delmo, Y. Wang, Y. Song, S. Zhu, H. Zhang, H. Xu, T. Li, J. Jang, Y. Kwon, Y. Wang, M. Shao, *J. Am. Chem. Soc.* **2024**, *146*, 1935; b) S. Zhu, B. Jiang, W.-B. Cai, M. Shao, *J. Am. Chem. Soc.* **2017**, *139*, 15664.
- [35] a) J. Hsu, A. M. Eid, C. Randall, M. S. E. Houache, Y. Abu-Lebdeh, H. A. Al-Abadleh, *Langmuir* **2022**, *38*, 14789; b) R. Kas, O. Ayemoba, N. J. Firet, J. Middelkoop, W. A. Smith, A. Cuesta, *ChemPhysChem* **2019**, *20*, 2904.
- [36] a) M. Gattrell, N. Gupta, A. Co, *J. Electroanal. Chem.* **2006**, *594*, 1; b) X. Nie, W. Luo, M. J. Janik, A. Asthagiri, *J. Catal.* **2014**, *312*, 108.
- [37] a) Y. Wang, H. Shen, K. J. T. Livi, D. Raciti, H. Zong, J. Gregg, M. Onadeko, Y. Wan, A. Watson, C. Wang, *Nano Lett.* **2019**, *19*, 8461; b) Z. Xie, Q. Wang, H. Yang, J. Feng, J. Chen, S. Song, C. Meng, K. Wang, Y. Tong, *Small* **2024**, *2401530*; c) Y. Hori, H. Wakebe, T. Tsukamoto, O. Koga, *Surf. Sci.* **1995**, *335*, 258; d) G. Zhang, Z.-J. Zhao, D. Cheng, H. Li, J. Yu, Q. Wang, H. Gao, J. Guo, H. Wang, G. A. Ozin, T. Wang, J. Gong, *Nat. Commun.* **2021**, *12*, 5745; e) S. T. Ahn, S. Sen, G. T. R. Palmore, *Nanoscale* **2022**, *14*, 13132.
- [38] W. J. Durand, A. A. Peterson, F. Studt, F. Abild-Pedersen, J. K. Nørskov, *Surf. Sci.* **2011**, *605*, 1354.
- [39] Y. Li, C.-Z. Huo, H.-J. Wang, Z.-X. Ye, P.-P. Luo, X.-X. Cao, T.-B. Lu, *Nano Energy* **2022**, *98*, 107277.
- [40] a) Z. Chen, T. Wang, B. Liu, D. Cheng, C. Hu, G. Zhang, W. Zhu, H. Wang, Z.-J. Zhao, J. Gong, *J. Am. Chem. Soc.* **2020**, *142*, 6878; b) Q. Lei, H. Zhu, K. Song, N. Wei, L. Liu, D. Zhang, J. Yin, X. Dong, K. Yao, N. Wang, X. Li, B. Davaasuren, J. Wang, Y. Han, *J. Am. Chem. Soc.* **2020**, *142*, 4213; c) A. Verdaguer-Casadevall, C. W. Li, T. P. Johansson, S. B. Scott, J. T. McKeown, M. Kumar, I. E. L. Stephens, M. W. Kanan, I. Chorkendorff, *J. Am. Chem. Soc.* **2015**, *137*, 9808; d) X. Feng, K. Jiang, S. Fan, M. W. Kanan, *J. Am. Chem. Soc.* **2015**, *137*, 4606.
- [41] F. Zhu, L. Shao, J. Wang, S. Deng, J. Hao, W. Shi, *Appl. Surf. Sci.* **2024**, *645*, 158912.
- [42] S. Shen, J. He, X. Peng, W. Xi, L. Zhang, D. Xi, L. Wang, X. Liu, J. Luo, *J. Mater. Chem. A* **2018**, *6*, 18960.
- [43] R. Zhao, Y. Wang, G. Ji, J. Zhong, F. Zhang, M. Chen, S. Tong, P. Wang, Z. Wu, B. Han, Z. Liu, *Adv. Mater.* **2023**, *35*, 2205262.